Unraveling the exhumation history of high-pressure ophiolites using magnetite (U-Th-Sm)/He thermochronometry

Stéphane Schwartz, Cécile Gautheron, Richard Ketcham, Fabrice Brunet, Marianna Corre, Arnaud Agranier, Rosella Pinna-Jamme, Frédéric Haurine, Gael Monvoin, Nicolas Riel

Unraveling the exhumation history of high-pressure ophiolites using magnetite (U-Th-Sm)/He thermochronometry

Stéphane Schwartz[1,2,*], Cécile Gautheron[2], Richard A. Ketcham[3], Fabrice Brunet[1], Marianna Corre[1], Arnaud Agranier[4], Rosella Pinna-Jamme[2], Frédéric Haurine[2], Gael Monvoin[2], Nicolas Riel[5]

[1] ISTerre, Univ. Grenoble Alpes, Univ. Savoie Mont Blanc, CNRS, IRD, IFSTTAR, 38041 Grenoble, France

[2] GEOPS, Univ. Paris-Sud, CNRS, Université Paris-Saclay, 91405 Orsay, France

[3] Jackson School of Geosciences, The University of Texas at Austin, Austin, TX, USA

[4] Laboratoire Domaines Océaniques, CNRS, IUEM, Université de Bretagne Occidentale, 29280 Plouzané, France

[5] Institute of Geosciences Johannes Gutenberg, University Mainz, D-55128 Mainz, Germany

* corresponding author: stephane.schwartz@univ-grenoble-alpes.fr

To be submitted to EPSL

Keywords: Thermochronometry; (U-Th-Sm)/He; Magnetite; Modeling; High-pressure ophiolites; Exhumation

Abstract

Magnetite is a ubiquitous oxide in ultramafic and mafic rocks, which is present in a large range of geological and tectonic settings. In the case of high-pressure ultramafic rocks, exhumation timing is commonly constrained by geochronometers in nearby lithologies. The development of the magnetite (U-Th-Sm)/He method (MgHe) has opened new perspectives to refine the exhumation history of such rocks. However no thermal history has been deduced using MgHe data so far. Here we applied MgHe dating to magnetite from an HP-LT alpine ophiolite body (Rocher Blanc) from the Schistes lustrés units (Western Alps, France) where part the P-T-t history is constrained to further refine the thermal history and demonstrate validity of the method. Textural and geochemical characterizations of the magnetite grains reveal two crystallization environments leading to distinct grain morphologies, euhedral and pseudo-euhedral, with different amounts of mineral inclusions (titanite, chlorite and augite-aegirine). Both magnetite types crystallized during the same retrograde path at T> 250°C, under hydrothermal conditions shown by Si and V oscillatory zoning and low Ti content. MgHe ages derived from euhedral magnetite crystals range from 14.8±2.1 to 20.9±3.0 Ma, between zircon and apatite fission track (ZFT) and (AFT) ages deduced from the literature. Pseudo-euhedral grains display older ages interpreted as resulting from the implantation of He from U-rich neighboring minerals such as titanite. For the first time, MgHe data are inverted along with AFT and ZFT data to refine the thermal history of an ophiolite related to their exhumation. The MgHe data suggest that the Rocher Blanc sample has undergone an exhumation in ductile conditions related to subduction dynamics and underplating processes, followed by an exhumation reflecting denudation by erosion under brittle conditions. This exhumation regime change is found to take place at ~20 Ma, as opposed to a less constrained ~26 Ma cooling as would be inferred from the ZFT

and AFT ages alone. Considering published thermochronometric data along the Western Alps, we propose that the exhumation is controlled by the upward indentation of the Apulian mantle producing regional tilting and associated erosion. With the present Schistes lustrés ophiolite example, we demonstrate that the MgHe method can be used as a low-temperature thermochronometer (closure temperature in the 200-250°C range) that aids in unraveling the cooling history associated with exhumation of high-pressure ultramafic and mafic rocks at the brittle to ductile transition.

1. Introduction

Ultramafic and mafic rocks are widely distributed on the Earth's surface and are associated with a large range of geological and geodynamic settings, from oceanic accretion to orogenic zones (e.g., Guillot et al., 2015). In contrast to their abundance, mafic and ultramafic rocks only yield a few minerals suitable for geo-thermochronometry such as U-Th-bearing accessory minerals (zircon, titanite or apatite). However, recent advances in the analysis of radiogenic isotopes have extended the application of (U-Th)/He geo-thermochronology to minerals incorporating U and Th at the ppb level such as magnetite (Blackburn et al., 2007; Cooperdock and Stockli, 2016) or spinel (Cooperdock and Stockli, 2018). Magnetite (U-Th)/He geo-thermochronometry, abbreviated MgHe below, opens new perspectives with respect to the use of basic and ultrabasic rocks for dating geodynamic processes.

Indeed, magnetite ($Fe^{2+}Fe^{3+}{}_2O_4$) is ubiquitous in these rock types where it can either crystallize from the parent magma or precipitate later in the rock history from hydrothermal fluids at lower temperature. The MgHe method is particularly attractive for dating geodynamic processes involving serpentinite formation, metamorphism or exhumation. Magnetite is produced during serpentinization of the lithospheric mantle at slow-spreading

ridges for T>200°C (Klein et al., 2013; Klein et al., 2014) and controls thereby hydrogen production (e.g., see Brunet, 2019 for a review). Magnetite in subducted serpentinite can survive temperature conditions up to the antigorite breakdown (Debret et al., 2014; Merkulova et al., 2017). Therefore, in addition to constraining the timing of mafic and ultramafic rocks exhumation, dating of magnetite by (U-Th-Sm)/He geochronometry can also put time constraints on the functioning of fossil hydrothermal systems and on serpentinite metamorphism in subduction-collision zones.

The MgHe method is based on radiogenic ^{4}He production and accumulation in the crystal lattice during alpha decay of U, Th, and Sm isotopes (^{238}U, ^{235}U, ^{232}Th and ^{147}Sm) that lead to stable isotopes (^{206}Pb, ^{207}Pb, ^{208}Pb and ^{143}Nd respectively). The alpha particle is ejected with a high kinetic energy of several MeV and travels a mean distance of ~15 µm in the magnetite lattice (Ketcham et al., 2011). A correction for He loss due to alpha ejection (called F_T) needs to be applied which can range from few percent to 20-30% for smaller grains with sizes of ~100 µm (Farley et al., 1996). Otherwise, abrasion of the first ~15 µm of the crystals or selection of the inner parts of a large crystal can be done to avoid ejection or implantation from neighboring minerals (Blackburn et al., 2007; Cooperdock and Stockli, 2016). The remaining He atoms in the crystal can diffuse outside of the crystal with a rate of diffusion that is a function of the temperature and crystal volume. Based on experimental He diffusion coefficients obtained on magmatic magnetite by Blackburn et al. (2007), the closure temperature Tc (Dodson, 1973) is as 250±40°C for a crystal size of 500 µm and a cooling rate of 10°C/Ma. The Tc for He in magnetite falls in the same range as for the zircon fission track (ZFT) system, which is broadly estimated to be ~240±50°C (Gallagher et al., 1998). Ketcham (2019) derived a Tc value of 281°C based on fitting experimental data sets from relatively

96 young zircons (Murakami et al., 2006), and Rahn et al., (2004) showed that radiation damage
97 may lower annealing resistance.
98 The number of studies dealing with the MgHe method remains limited. MgHe has been
99 applied to volcanic rocks (Blackburn et al., 2007), ore deposits (Fanale and Kulp, 1962) as
100 well as serpentinites and chloritoschists (Cooperdock and Stockli, 2016). These studies have
101 clearly demonstrated the relevance of the MgHe thermochronometer to obtain cooling or
102 crystallization ages. However, MgHe data have never previously been used to infer the
103 thermal history of rocks using inverse modeling, which is the main purpose of collecting
104 thermochronometric data.
105 Here, the MgHe method is applied to an ophiolite from the Schistes lustrés units (Western
106 Alps, France), for which the cooling history is relatively well constrained, as the mineralogy
107 and P-T history of the area have been characterized (Pognant and Kienast, 1986; Tricart and
108 Schwartz, 2006) and ZFT and AFT data are available (Schwartz et al., 2007). The obtained
109 MgHe data are critically evaluated in the framework of the ophiolite thermal history
110 constrained by the ZFT and AFT literature data.
111
112 **2. Geological setting**
113 The studied samples were collected in the internal domain of the western Alps (Fig. 1A) that
114 underlies the boundary between the European and African plates (e.g., Lemoine et al., 1986).
115 This domain (Fig. 1B) derives from a part of the Tethyan ocean (Piedmont zone) and its
116 northwestern European margin (Briançonnais zone). In the study area, the Piedmont zone is
117 composed of the Schistes lustrés units and the Monviso ophiolite, which rest on the internal
118 crystalline massif of Dora Maira (Fig. 1C). These units were juxtaposed during subduction
119 and collision processes in Late Cretaceous to Late Tertiary times. The Piedmont zone

120 represents different levels of a paleo-subduction zone, preserving the low thermal gradient
121 (5–8°C/km) associated with the subduction dynamics (Schwartz et al., 2001; Agard et al.,
122 2002). In this context, the Schistes lustrés units correspond to a fossiliferous sedimentary
123 accretionary wedge metamorphosed under high pressure and low temperature (HP-LT)
124 conditions during the late Cretaceous–early Eocene subduction of the Tethyan ocean (Lafay
125 et al., 2013). This domain is derived from Mesozoic oceanic sediments that were originally
126 composed of marls, clays, and limestones associated with fragments of oceanic lithosphere.
127 These sediments were strongly deformed and metamorphosed during subduction, and they
128 crop out today as foliated and polydeformed calcschists enclosing boudinaged meter- to
129 kilometer-sized Jurassic ophiolites. The P-T conditions increase toward the east, from low-
130 temperature blueschist (LT-BS, Fig. 1C) to high-temperature blueschist facies conditions (HT-
131 BS, Fig. 1C) (Tricart and Schwartz, 2006). The blueschist domain is structurally located above
132 the Monviso eclogitic ophiolite (Fig. 1C). In this massif, the metasedimentary component is
133 small (<20 vol.%) relative to the voluminous oceanic lithosphere (Schwartz et al., 2001).
134 The P-T evolutions of the Schistes lustrés units are well documented and show clockwise
135 loop paths, keeping a record of the early prograde evolution, and the retrograde
136 metamorphism stages have remained in the field typical of greenschist paragenesis (Fig. 1D),
137 with no temperature increase (Tricart and Schwartz, 2006). For the studied Rocher Blanc
138 ophiolite located in the central part of the Schistes lustrés units (Fig. 1C), the metamorphic
139 peak conditions are estimated at 10±2 kbar and >350°C (Tricart and Schwartz, 2006,
140 Schwartz et al., 2013), with laser probe Ar-Ar ages ranging from 62 to 55 Ma (Agard et al.,
141 2002). The final exhumation is constrained by apatite and zircon fission track (AFT-ZFT)
142 analysis (Schwartz et al., 2007) (Fig. 1C), which reveals a diachronous exhumation of the HP-
143 LT metamorphic rocks from east to west during Oligocene to Miocene time. Taking into

account the cooling rates from Schwartz et al. (2007), the Rocher Blanc ophiolite is considered to have passed through the ~240-280°C isotherm at 24.8±1.6 Ma and the ~110°C isotherm at 12.3±2.0 Ma (Fig. 1C).

3. Samples and methods

3.1. Sampling and petrologic characterization

Sample RB1 was collected from the Rocher Blanc massif (RB; WGS84 UTM31N, 6°57'08.01''E, 44°39'53.25''N; elevation: 2810 m a.s.l.) that corresponds to a km-scale ophiolitic body composed of mafic and ultramafic rocks embedded in the Schistes lustrés units (Fig. 1C) that record middle-temperature blueschist facies conditions (MT-BS) (Pognant and Kienast, 1986; Tricart and Schwartz, 2006). The high-pressure blueschist paragenesis in mafic rocks (glaucophane, zoisite) has been partially to totally retrogressed at greenschist facies conditions (chlorite, titanite and augite-aegirine). In ultramafic rocks, high pressure is characterized by the presence of antigorite (Schwartz et al., 2013). The studied sample (RB1) corresponds to a magnetite-bearing chloritized Fe-Ti meta-gabbro (chloritoschist), some tens of centimeters thick, located at the interface between meter-size lenses of Fe-Ti gabbro and serpentinite (Fig. 2A). The sample contains visible mm-scale euhedral magnetite crystals as shown in Figure 2B, which are superimposed over the main schistosity defined by the chlorite – titanite assemblage (Fig. 2C).

3.2. Mineralogical and geochemical analysis

The chemistry of both euhedral and pseudo-euhedral magnetite crystals of the RB1 sample were characterized at the microscale. Semi-quantitative analyses and imaging of five magnetite and their inclusions were performed with quantitative analyses and mapping of

minor and trace elements in magnetite (Si, Ti, Cr, V, Mn and Mg). Several SEM images are shown in Figures 2D, E, F, and concentrations of Si, Ti, Sr, V, Mn, and Mg obtained on magnetite crystals are reported in Table 1. Figure 3 presents the Si and V contents of one euhedral and one pseudo-euhedral magnetite crystal identified also in Figure 2C. Additional information can be found in the supplementary section.

In-situ uranium and thorium concentrations in chlorites, titanites and magnetites from sample RB1 were quantified by laser ablation inductively coupled plasma mass spectrometry (LA-ICPMS). Results are presented in Table 2 and on Figure 4. Nevertheless, 2σ internal errors are reported in Table 2 and additional details can be found in the supplementary section.

3.3. Crystal selection using CT scanning

Magnetite grains scans were performed following guidelines by Cooperdock and Stockli (2016, 2018), and addition details can be found in the supplementary section. The blob3D software (Ketcham, 2005a; Cooperdock et al., 2019) was used to determine precisely the volume, surface/volume ratio, sphere-equivalent radius and alpha-ejection factor F_T (Ketcham et al., 2011) for each grain, and the presence of large inclusions (>5 µm). 3D images of the magnetite crystals were generated to aid in selecting crystals for (U-Th-Sm)/He dating and documenting their euhedral and pseudo-euhedral shapes. 3D grain shape images of MgHe-analyzed magnetite crystals are reported in Figures 5A and B.

3.4. (U-Th-Sm)/He on magnetite

Non-abraded single mm-size euhedral and pseudo-euhedral magnetite crystals were degassed under-vacuum in order to determine the He content using the protocol described

192 in Allard et al. (2018). He content is corrected from the blank level, which is from 40 to 160
193 times lower than the He signal. Helium content error is estimated to 2% accordingly. The wet
194 chemistry digestion protocol was adapted from Blackburn et al. (2007) allowing the
195 determination of the ^{238}U, ^{232}Th, ^{147}Sm content. Additional details are placed in the
196 supplementary section. Analytical uncertainties in the U, Th and Sm content translate into a
197 15% error on alpha-ejection-corrected MgHe ages. Sample mass, volume, He, U, Th, Sm
198 content, raw and alpha-ejection-corrected (U-Th-Sm)/He ages are reported in Table 3.
199
200 **4. Results**
201 **4.1. Magnetite phase relationships and chemical composition**
202 At the thin section scale, magnetite crystallizes in two zones of distinct mineralogy, which
203 are likely inherited from the initial distribution of magmatic minerals in the Fe-Ti gabbro (Fig.
204 2C). The mineralogy of these two zones is either dominated by a chlorite + magnetite ± relict
205 magmatic pyroxene (Zone 1) or titanite + magnetite ± chlorite ± relict magmatic ilmenite
206 (Zone 2) assemblages. In Zone 1, the augite-aegirine pyroxene may stably coexist with
207 titanite and chlorite contains a 10-20 % jadeitic component. In Zone 2, titanite, magnetite
208 and chlorite appear texturally as destabilization products of magmatic ilmenite and
209 generates local reaction coronas (Fig. 2D). Plagioclase has not been identified in either of the
210 two zones. Magnetite crystal habits differ between the two zones. In Zone 2, magnetite is
211 pseudo-euhedral to anhedral, possibly polycrystalline, and contains numerous inclusions (Fig.
212 2D-E) of titanite and chlorite. In Zone 1, magnetite is euhedral, and can form larger grains
213 exceeding 500 µm with rare inclusions (Fig. 2F) of augite-aegirine, chlorite and titanite.
214 Chemical characterization of euhedral magnetite crystals from Zone 1 and pseudo-euhedral
215 magnetite crystals from Zone 2 are reported in Table 1. Significant Mn, Cr and Ti contents

are present but remain below 500 ppm (Table 1). Mg is below detection limit (i.e., <25 ppm), while Si and V are the two most concentrated cations after Fe, with mean concentrations of 809±513 and 1821±265 ppm, respectively (Table 1). The Si and V distribution patterns are the same in euhedral and in pseudo-euhedral magnetite grains indicating similar growth process and history. It is characterized by oscillatory zoning with a relatively good correlation between Si and V-rich growth zones (Fig. 3), although vanadium zoning is sharper. The nature of the inclusions and their distribution seem independent of the chemical variations recorded by these two elements.

4.2. Magnetite, chlorite and titanite in-situ U content

The U content of magnetite derived from laser ablation ranges from 5±0.4 to 24±16 ppb and is ~five times higher in the rim compared to the core (Table 2, Figure 4). In addition, the U content is similar to the U value obtained by wet chemistry for the dated crystals with value of 8±1 to 29±2 ppb (Table 3). The U content is also similar between magnetite from Zone 1 (euhedral) and Zone 2 (pseudo-euhedral) (Table 2 and 3). The U content in chlorite from Zone 1 of ~16±8 ppb is lower than the content in chlorite from Zone 2 which ranges from 42±5 to 68±10 ppb (Table 2, Figure 4). Although variable, the U content of titanite is by far the highest with values ranging from 27±5 to 1569±141 ppb. In the RB1 sample titanite is the U-bearing phase.

4.3. Magnetite (U-Th-Sm)/He

Five euhedral magnetite crystals (Fig. 5A) and two pseudo-euhedral grains (Fig. 5B) were selected for MgHe dating, utilizing the CT scan data to select grains with the fewest (for pseudo-euhedral magnetite) or no inclusions. The selected crystals have equivalent-sphere

radii (Rs) ranging from 362 to 483 µm (Table 3). Helium content of these seven magnetite grains ranges from 0.9 to 3.3 pmol/g and effective uranium (U+0.24Th) ranges from 9 to 34 ppb (Table 3). Ejection-corrected MgHe ages for euhedral and pseudo-euhedral grains range from 14.8±2.1 to 20.9±3.0 Ma and 30.4±4.4 to 32.0±4.6 Ma, respectively (Fig. 5C).

5. Discussion

5.1. Conditions of magnetite formation

Magnetite is a common mineral in ultramafic and mafic rocks and appears over a large range of P-T and fO_2 conditions (Nadoll et al., 2014). In the case of magnetite created during the oceanic serpentinization process, it is classically assumed to form at temperatures above ~200°C (e.g., Alt et al., 2013; Klein et al., 2013; Klein et al., 2014), even if magnetite could potentially crystallize at temperatures even below 120°C (Alt et al., 2013). In the case of subducted ophiolites (serpentinite and gabbro lithologies), magnetite is observed from eclogite paragenesis (Li et al., 2004; Debret et al., 2014) up to greenschist facies conditions related to the retrograde stage for temperatures ranging from 550 to 250°C (Schwartz et al., 2013).

The petrological and geochemical studies of the RB1 sample indicate that the euhedral and pseudo-euhedral magnetite grains crystallized during the retrograde path under greenschist facies conditions assisted by metamorphic hydrothermal fluids and are not derived from magmatic origin. Indeed, the Ti content of magnetite crystals is under 100 ppm (Table 1), too low to be of magmatic origin (Nadoll et al., 2014), and the host inclusions (titanite, chlorite, augite-aegirine) that are representative of HP-LT paragenesis demonstrate that magnetite grains crystallized during the greenschist retrograde path. In this context, the oscillatory V and Si chemical zoning, with a Si-richer rim observed for euhedral and pseudo-euhedral

magnetite grains (Figure 3) record the changing conditions and compositions of the metamorphic fluid related to magnetite growth (Dare et al., 2014). The Si and V are the main minor elements at the ~1000 to 2000 ppm level, compared to Ti, Cr, Mn, and Mg (Table 1); these Si and V contents reveal high solubility indicating crystallization from a high temperature fluid (Dare et al., 2014). Such high Si content has already been encountered in hydrothermal systems (skarns, metamorphic veins; e.g., Shimazaki, 1998) and Si oscillatory zoning has been described in hydrothermal magnetite (Deditius et al., 2018). Hydrothermal conditions (250-350°C, Fig. 6A) in the fluid-circulation zone marked by the magnetite-bearing chloritoschists may have favored Si and V incorporation, the latter element being supplied locally by the Fe-Ti gabbro itself.

Based on previous thermobarometric studies of the host metamorphic Fe-Ti gabbro (e.g., Pognante and Kienast, 1986), and petrological investigation in this study, the magnetite begins to crystallize most probably near the blueschist – greenschist transition, as residual augite-aegirine is found in inclusions, and magnetite crystallization continues during the entire greenschist retrograde path (Fig. 6B).

5.2. Magnetite He age distribution

The MgHe ages for all crystals are younger than the high-pressure ages recorded for the Schistes lustrés units (62-54 Ma; Agard et al., 2002), and potentially represent exhumation ages, i.e., related to the retrograde path. Interestingly, the euhedral grains are quite homogeneous with a mean age of 18.1±2.4 Ma that falls between the AFT and ZFT ages as deduced from Schwartz et al. (2007) for the Rocher Blanc area (Fig. 5C), and are thus compatible with cooling ages associated with the exhumation history of the area. Indeed, the MgHe ages are younger than ZFT ages, and older than AFT ages, in agreement with the

published thermal sensitivity of MgHe (250±50°C; Blackburn et al., 2007), ZFT (240±50°C, Gallagher et al., 1998; ~281°C, Ketcham, 2019) and AFT (110±10°C, Gallagher et al., 1998). Conversely, the ages obtained on pseudo-euhedral crystals are significantly older than the euhedral crystal and ZFT ages (Fig. 5C). This is not consistent with petrological data which show that euhedral and pseudo-euhedral magnetite all crystallized simultaneously under greenschist conditions at T > 250°C. Thus, we interpret these ages as related to the presence of excess He compared to euhedral crystals with similar size and eU content (Table 3); they cannot be considered as cooling ages. Excess of He may be due to (i) the impact of alpha implantation from neighboring minerals or circulating rich U-Th fluids, and/or (ii) the impact of inclusions with higher U-Th content on the global He budget of magnetite.

Alpha implantation has been frequently observed or modeled for the (U-Th)/He method, especially for apatite (e.g., Spiegel et al., 2009; Gautheron et al., 2012) and magnetite (Blackburn et al., 2007; Cooperdock and Stockli, 2016). When minerals contain lower or equivalent U and Th content compared to neighboring phases, the alpha implantation effect can be significant. This is particularly the case for magnetite, which typically contains low U-Th content (<30 ppb) compared to minerals with high U-Th content of >100 ppb like titanite in the present case (Table 2). In Zone 1, magnetite is embedded in chlorite which is U-poor with contents ~15 ppb. It must be noted that the higher U content in Zone 2 results in a higher U content, from 40 to 60 ppb, in chlorite as well (Table 2, Figure 4). In the RB1 sample, for the chlorite area (Zone 1) alpha implantation in magnetite should be negligible whereas in the titanite area (Zone 2) alpha implantation in magnetite could be significant. As the RB1 grains are large (Rs >400 µm) with small alpha ejection corrections (F_T>0.97; Ketcham et al., 2011), a 20-40 ppb matrix would simply cancel out the F_T correction, and only thousands of ppb U-Th will have an age effect approaching 10% (Gautheron et al., 2012). For euhedral

312 magnetite, MgHe ages younger than ZFT imply no significant alpha implantation and
313 reinforce the hypothesis that euhedral magnetites crystallized in Zone 1 (chlorite-rich
314 environment). Similarly, MgHe ages older than ZFT observed for the pseudo-euhedral
315 magnetite may reflect implantation from U-Th-rich neighboring minerals such as titanite,
316 consistent with the pseudo-euhedral magnetites crystallizing in Zone 2, in agreement with
317 petrological observations.
318 Inclusions richer in U-Th than the host minerals can also impact (U-Th)/He ages by adding He
319 to the crystal lattice, as already reported for apatite (Farley, 2002) and magnetite (Blackburn
320 et al., 2007; Cooperdock and Stockli, 2016). An excess of He can occur if the total U-Th
321 content of host mineral and inclusions is incompletely retrieved by the chemical digestion
322 protocol that is usually designed to target the host mineral. For magnetite, the digestion
323 protocol is not adapted to dissolve completely silicates (e.g., chlorite, titanite, zircon) or
324 other oxide minerals (e.g., titanite). A small fraction of the U-Th budget coming from
325 inclusions may be retrieved, but the total U-Th budget is incomplete, leading to spuriously
326 older MgHe ages with no geological significance. For the two pseudo-euhedral magnetites
327 from RB1, the MgHe ages older than the euhedral magnetites with similar U-Th content
328 (Table 2) would be consistent with the absence of U-Th-rich inclusions in the euhedral
329 crystals. However, because the CT scan analysis indicated minimal detectable inclusions, and
330 because the primary U-Th-bearing phase, titanite, has eU compositions only ~100x higher
331 than the magnetite (Table 2, 3), we do not believe inclusions can explain the magnitude of
332 excess He. We thus interpret that MgHe ages older than ZFT reflect implantation across
333 large areas of grain boundaries shared with titanite (Fig. 4D), and for the rest of the
334 discussion we do not use or further discuss the two pseudo-euhedral crystals, as their
335 measured ages are not geologically meaningful. However, we can conclude that the MgHe

ages from the euhedral crystals of the RB1 sample are not significantly impacted by implantation and reflect cooling due to exhumation along the retrograde path.

Finally, the results of this study give some methodological insight into MgHe dating. First, CT imaging is essential for detecting the presence of mineral inclusions larger than ~5 μm, as already stated by Cooperdock and Stockli (2016). Comparison of U-Th content for crystals with older MgHe ages can provide indirect evidence of the impact of rich U-Th inclusions below the CT-scan detection limit (<1 μm). Second, the removal of the 20 μm outer margin of the magnetite crystals, as recommended by Blackburn et al. (2007), is not always necessary. In fact, the result of this study shows that implantation is not always significant and depends on the petrological environment of magnetite (i.e. chlorite versus titanite zones), as well as the size of the crystal. Furthermore, alpha implantation along long grain boundaries shared with titanite, as documented in our zone 2 non-euhedral magnetites, if combined with diffusional migration of helium into the magnetite grain (Gautheron et al. 2012) may render abrasion an insufficient remedy, depending on cooling history. Thorough petrological characterization of mineral textures and compositions thus appears to be a necessary step of the MgHe method.

5.3. Origin of MgHe age dispersion

Significant MgHe age dispersion is encountered for euhedral RB1 magnetites (MgHe age = 18.1±2.4 Ma, 13% at 1σ). MgHe age dispersion has also been reported in previous work in the HP-LT subduction complex on the island of Syros, Greece (Cooperdock and Stockli, 2016). This age dispersion is higher than typical analytical error (i.e. ~5-10 %, for apatite and zircon) but similar or lower than frequently found in practice for apatite or zircon (U-Th)/He methods (e.g., Ault et al., 2019; Ketcham et al., 2018). Using investigations already published

360 on the origin of apatite or zircon (U-Th)/He age dispersion, some factors affecting MgHe
361 ages related to the impact of (i) U-Th zonation, (ii) slight alpha-implantation, or (iii) crystal-
362 dependent He diffusion coefficient can be anticipated.
363 First, a slight impact of alpha-implantation could affect the MgHe age, as the U-Th content of
364 the neighboring minerals could be slightly different For example, U and Th content for
365 chlorite of ~15 ppb has been determined for Zone 1 (Table 2), but slightly higher U-Th values
366 are possible (Table 2). However, the large crystal size of the magnetite from this study
367 reduces the impact of implantation. Nevertheless, other parameters can account for
368 dispersion. For instance, Cooperdock and Stockli (2016) found similar MgHe age dispersion
369 on abraded crystals (i.e. mechanical removal of the 20 µm border of the crystal that can
370 have been affected by alpha implantation).
371 Second, due to the low U-Th content, analytical determination of zoning is difficult, and up
372 to a ~4x higher U concentration in the rim has been measured for three magnetite crystals
373 (Table 2). Because the ablation spot is large (150 µm), the exact size of the U-Th-enriched
374 rim is not known but can be similar to the one observed by Si-V analysis, i.e. ~100 µm (Fig. 3).
375 In this case, the presence of a ~100 µm enriched U-Th rim will not have much impact on the
376 ejection factor as it is much larger than the mean stopping distance (15 µm). If finer zoning
377 exists, modeling can be performed (e.g., Farley et al., 1996; Gautheron et al., 2012) assuming
378 that U-Th zoning follows Si and V zoning (Fig. 3C and D). Using the Monte Carlo code
379 associated with Gautheron et al. (2012), we modeled a 400-µm radius sphere with a 50 µm
380 rim depleted or enriched in U-Th by 50%, and as a worst-case scenario a rim containing all of
381 the crystal's U-Th (i.e., no U-Th in the core). We obtained F_T ejection factors of 0.99, 0.96,
382 and 0.76, respectively, implying a 25% MgHe age difference for the worst case. However, in
383 comparing our bulk and in situ core and rim analyses we find no evidence of such severe

zoning in U-Th, and we can estimate a maximum MgHe age dispersion component of only up to a few percent. Given that implantation can be from minerals with much more than 50% higher eU, it is likely to be a source of equal or greater dispersion.

Third, a defect- and/or composition-dependent He diffusion coefficient could also be invoked to explain age dispersion, as has been proposed and modeled for other minerals such as apatite and zircon (Gautheron et al., 2009; Flowers et al., 2009; Guenthner et al., 2013). Indeed, damage due to radioactivity, and also crystal defects could trap or facilitate He diffusion within the crystal structure. A damage content of some 5% would be required to change the He diffusion coefficient significantly, as modeled for apatite (e.g., Gerin et al., 2017), which is unlikely given the low eU content of magnetite (<<1%). Alternatively, substitution by minor or trace elements could deform the crystal structure and thus modify He diffusion, as shown in apatite at the atomic scale (Djimbi et al., 2015). The magnetite crystals from RB1 have ~0.5 wt% of minor elements, and if we assume similar effect as for apatite (Djimbi et al., 2015), no significant change in the closure temperature compared to pure magnetite is expected. This is highly speculative, as the composition of the volcanic magnetite used by Blackburn et al. (2007) is not known. The effect of minor elements in magnetite on He volume diffusion still needs to be investigated. It is also possible that fluid inclusions can act as traps for He, as has been proposed for apatite and zircon (Zeitler et al. 2017; Danišík et al., 2017); this possibility could be further pursued with higher-resolution imaging and/or ramped heating experiments (McDannell et al., 2018).

Finally, we stress that there is currently only one experimental study documenting He diffusion kinetics in magnetite (Blackburn et al., 2007), and even that data set shows signs of complex release behavior. Further data are certainly required to build a more robust database of kinetic parameters and explore possible anomalous behaviors.

408

409 **5.4. MgHe data inversion: resolving exhumation rate from the Rocher Blanc ophiolite**

410 The petrological and geochemical arguments deduced from the RB1 sample analysis indicate
411 that magnetite crystalized at T> 250°C, as illustrated in Figure 6, at temperature higher than
412 the MgHe closure temperature (Tc), and thus that MgHe ages obtained from euhedral
413 magnetite of ca. 18.1±2.4 Ma correspond to cooling ages of the Rocher Blanc ophiolite (Fig.
414 6). Specifically, for the dated RB1 magnetites, which all have similar sizes (Table 3), Tc ranges
415 from 242 to 248°C for sphere-equivalent radii of 362 to 483 µm and a cooling rate of
416 10°C/Ma. MgHe ages derived from are sandwiched between ZFT and AFT ages as expected
417 by their thermal sensitivity, and in fact shed further light on the thermal sensitivity of the
418 ZFT method, supporting a ZFT Tc >260 °C. Figure 6 summarizes the P-T path for RB1 sample,
419 including the magnetite growth field during the retrograde path and the time constraint
420 obtained from AFT, ZFT and MgHe ages.

421 ***5.4.1. MgHe data inversion***

422 The thermal history of the studied area was retrieved using the HeFTy software (Ketcham,
423 2005b) by inverse modeling of MgHe, AFT and ZFT low temperature thermochronometric
424 data. HeFTy uses a constrained Monte Carlo scheme that poses a large number of candidate
425 time-temperature (t-T) paths, and retains those that fit the thermochronometric data to a
426 “good” (closer than statistical expectation for a random sample) or “acceptable” (does not
427 fail a 95% confidence test) extent. For the inversions the fission-track annealing models by
428 Ketcham et al. (1999) and Ketcham (2019) were used for AFT and ZFT data, respectively. For
429 MgHe ages, the sphere-equivalent radii (Rs) of each crystal and He diffusion parameters
430 from Blackburn et al. (2007) were used. In detail, the HeFTy software models (i) the fission-
431 track production and annealing in apatite and zircon, and (ii) helium production, taking into

account ejection and diffusion, in magnetite. In this way, the data inversion identifies a family of potential cooling histories by using 17 t-T nodes randomly placed to define a cooling-only path with a maximum allowed cooling rate of 50°C/m.y. over any segment. In addition to the MgHe, AFT and ZFT data, the peak HP-LT metamorphic conditions for the Rocher Blanc ophiolite massif as reported in Figure 6, estimated to be 350±20°C at 58±4 Ma (Agard et al., 2002) is used at a starting point. Further model inputs are listed in Table 4.

Thermal history modeling was performed with AFT-ZFT alone, with MgHe data alone and with all three combined (AFT-ZFT and MgHe). First, modeling was done with interpolated AFT and ZFT ages for RB1 sample assuming that ages vary linearly with the sample position on a W-E transect (Schwartz et al., 2007) (Fig. 1), and with and without MgHe data. Second, inversions were also performed with AFT and ZFT data from RN and CG samples, that represent the available data geographically framing the RB ophiolite (Fig. 1C), and with and without MgHe data. Finally, for comparison, the AFT-ZFT data and the MgHe data separately for RB1 sample were inverted. For modeling of MgHe data, all euhedral grains were individually included. The computed thermal histories are reported on Figure 7. In the on-line supplement, Figure S1 presents the modeling inversion results obtained for AFT and ZFT data of CG and RN samples.

5.4.2. Thermal history modeling

The inversion of the MgHe data alone or with the AFT and ZFT literature data allows us to refine the final t-T exhumation history of the Rocher Blanc ophiolite massif, while also verifying good consistency with AFT and ZFT data. First, model outputs showing the set of good and acceptable fits, and their weighted mean, demonstrate that the MgHe data provide time constraints at ca. 230-240°C (Fig. 7A) whereas ZFT and AFT ages put constraints

456 on the Rocher Blanc ophiolite cooling history at ~280 and ~100°C (Fig. 7B) respectively. In
457 particular, the MgHe data refine the thermal history by requiring that the rapid phase of
458 cooling did not commence until after 20 Ma (Fig. 7C). The three systems are thus
459 complementary with respect to the temperature range that they cover. The apparent
460 consistency between MgHe, AFT and ZFT cooling ages suggests that the He diffusion data
461 obtained at 1 bar by diffusion experiments in vacuum at temperatures between 350 and
462 620°C over several days by Blackburn et al. (2007) can be extended to geological conditions
463 and timescales. As the AFT and ZFT data for RB1 sample are extrapolated from a different
464 locality, we also ran models with AFT and ZFT ages from samples CG and RN (Fig. S1). The
465 resulting cooling histories only slightly differ from those obtained with the extrapolated
466 Rocher Blanc ophiolite ages (Fig. S1) supporting the relevance of this thermal modeling
467 approach.
468
469 **5.5. Final exhumation of the Rocher Blanc ophiolite: geodynamic implications**
470 The thermal history obtained using the combination of thermochronometric methods (AFT-
471 ZFT and MgHe data) brings strong constraint on the final exhumation of the Rocher Blanc
472 ophiolite and also on the Schistes lustrés units of the Piedmont zone (Western Alps). Our
473 thermal modeling reveals that the RB1 sample has undergone nonlinear cooling and records
474 a major change in the thermal pathway at 20 Ma (Fig. 7C). During the first exhumation stage,
475 from 55 to 20 Ma, the sample recorded slow cooling from 350 to 300 °C associated with an
476 extensive exhumation from 30 to 10 km (Fig. 6). The exhumation of ~20 km of rocks from
477 the Alpine orogenic wedge cannot be accounted for by surface denudation (i.e. erosion) only.
478 Large exhumation with limited cooling rather corresponds to exhumation in ductile
479 conditions related to subduction dynamics and underplating processes (Agard et al., 2001).

During ductile exhumation the sample passes from blueschist to greenschist conditions with a mean exhumation rate lower than 1 mm/yr, calculated using the depth and time constraints (Fig. 6A and 7). Over the second exhumation stage, from 20 Ma to 10 Ma, the RB1 sample records rapid cooling from 300 to 100°C (Fig. 7) associated with an exhumation from 10 to 3 km (Fig. 6A). This exhumation and strong change of cooling rate reflect denudation in the brittle conditions. A mean exhumation rate of 0.7 mm/yr can be deduced (Fig. 6A and 7). The last information of the thermal history is given by the final exhumation stage recorded by AFT data and an exhumation of 3 km over 10 Ma leading to a mean lower exhumation rate of 0.3 mm/yr (Fig. 7). Interestingly, the sample records similar exhumation rate in ductile and brittle domains around <1 mm/yr, but significant cooling rate variations. The change at ~20 Ma corresponds to the passage of the Rocher Blanc ophiolite below the transition from ductile to brittle conditions in the lower grade of the greenschist facies conditions (~250°C) during the retrograde path.

The final exhumation recorded by the thermal history reflects denudation at brittle conditions (Fig. 7), where denudation is related to erosion linked to relief creation. The relief creation is associated to a westward tilting of the Schistes lustrés units (Tricart et al., 2004; Schwartz et al., 2009), as a response to the upward indentation of the Dora Maira massif. Indeed, the crustal scale geometry of the internal zone is characterized by the presence of Apulian mantle in a superficial position (Fig. 8), at 12 kilometers below the Dora Maira massif (Lardeaux et al., 2006; Zhao et al., 2015). This portion of cold and rigid mantle acts as an indenter that allowed the deformation of the thinned Briançonnais margin by crustal underthrust process constituting a continental subduction wedge that forms the current basement of the Piedmont zone (oceanic subduction wedge in Fig. 8). This continental

503 subduction wedge was overthrust on the European crust by the activation of the crustal
504 Penninic Frontal Thrust (PFT in Fig.8) at ~34 Ma (Dumont et al., 2012).
505 Taking in consideration the MgHe data of this study, the AFT-ZFT data of Piedmont zone
506 (Schwartz et al., 2007) and AFT data of the internal crystalline Massif of Dora Maira (Beucher
507 et al., 2012), we can illustrate the evolution of the area with their respective positions
508 though time in the orogenic wedge (Fig. 8). At present-day, all samples crop out at similar
509 elevations (>2000 m a.s.l.) for the Piedmont zone and at lower elevation (<1500 m a.s.l.) for
510 Dora Maira. At present-day the global shortening affects the front of the European foreland
511 (Schwartz et al., 2017), and allows the uplift and exhumation of the external crystalline
512 massifs (Pelvoux, Beucher et al., 2012) (Fig. 8). Using the AFT-ZFT and MgHe ages and
513 thermal sensitivity of the thermochronometric systems for all the samples, we can
514 reconstruct their position at depth ~20 Ma ago. Firstly, the samples CR from Schistes lustrés
515 and from Dora Maira present AFT age of 20-25 Ma indicating a shallow position around 3 km
516 (assuming an AFT closure temperature of 100°C and a thermal gradient of 25 °C). The
517 position at depth for the other samples from the Piedmont zone need to be progressively
518 deeper from east to west (Fig. 8). RB1 sample was passing the 250°C isotherm ~20 Ma based
519 on the thermal history obtained in this study (Fig. 7). From ~20 Ma to present-day, the
520 Piedmont zone has recorded a differential exhumation with a westward titling and uplift
521 that is recorded by the youngest ages to the east in the Monviso (Fig. 8). This exhumation is
522 controlled by the upward indentation of the Apulian mantle producing the global tilting of
523 the Piedmont zone (Fig. 8).
524

525 **6. Conclusions**

526 This study contributes to the understanding of the formation conditions of magnetite in HP-
527 LT ophiolite and to the use of magnetite (U-Th-Sm)/He as a thermochronometer to quantify
528 the exhumation history. We demonstrate that a comprehensive characterization of
529 magnetite crystals and crystallization environment is needed in conjunction with MgHe
530 dating in order to interpret the age data.
531 We specifically focused on one sample (RB1) from the Rocher Blanc massif that is an
532 ophiolitic body embedded in the Schistes lustrés units (Western Alps, France), which
533 contains abundant magnetite. This sample recorded middle-temperature blueschist facies
534 conditions and was overprinted by greenschist conditions during exhumation. We show that
535 for the RB1 sample, magnetite crystallized in two zones of distinct chemistry, that originated
536 from magmatic relictual zones, with euhedral and pseudo-euhedral grains with a dominant
537 chlorite or titanite mineralogy, respectively. In addition, the petrological and magnetite
538 geochemical analyses (e.g. V and Si) indicate that magnetite crystallized during the
539 retrograde metamorphic path under greenschist conditions (T> 250°C). The Si and V zoning
540 observed in euhedral and pseudo-euhedral magnetite grains reinforce the fact that both
541 type of magnetite crystallized under same physical conditions. The pseudo-euhedral
542 magnetite, crystallizing in dominant titanite mineralogy, present older MgHe ages compared
543 to euhedral magnetite. The old MgHe ages are interpreted by the impact of alpha-
544 implantation from U-Th-rich neighbor minerals (e.g., titanite). On the contrary, alpha-
545 implantation in euhedral magnetite crystallizing in chlorite dominant zone is insignificant, as
546 chlorite contain similar U-Th content than magnetite. The MgHe ages derived from euhedral
547 magnetite range from 14.8±2.1 to 20.9±3.0 Ma, sandwiched between ZFT and AFT ages as
548 expected. The MgHe data along with AFT and ZFT data were inverted for the first time to
549 refine the local thermal history. The MgHe data suggest that fast cooling was delayed until

~20 Ma, as opposed to the less constrained ~26 Ma that would be inferred from the ZFT and AFT ages alone. The MgHe data suggest that the RB1 sample has undergone an exhumation in ductile conditions related to subduction dynamics and underplating processes, followed by an exhumation reflecting denudation by erosion at brittle conditions. Considering all thermochronometric data along the Western Alps, we propose that the exhumation is controlled by the upward indentation of the Apulian mantle producing the global titling of area and associated erosion.

Additional work on U-Th zoning in magnetite and He diffusion in magnetite will be necessary in the future, as the thermal inversion interpretation is contingent on the Blackburn et al. (2007) kinetic parameters being correct. Nevertheless, the present study further demonstrates that MgHe can be used as a low-temperature thermochronometer to date HP ultramafic final exhumation and the ductile-brittle transition opening new avenues of research. This method effectively complements the available thermochronological tools, making it a powerful tool for emerging applications.

Acknowledgments

This work has been funded thanks to TelluS-SYSTER INSU 2016 project and CNRS Delegation of S. Schwartz. The UTCT lab is supported by NSF-EAR-IF grant EAR-1762458 to R. Ketcham. Jessie Maisano is thanked for her help during CT scanning. V. Batanova, V. Magnien and N. Findling are thanked for the technical support of microprobe and SEM analysis. B. Guéguen is warmly thanked for her help during the magnetite chemical dissolution part. The three anonymous reviewers and An Yin editor are warmly thanked for their constructive reviews.

References

Agard, P., Jolivet, L., and Goffé, B., 2001. Tectonometamorphic evolution of the Schistes Lustrés complex: implications for the exhumation of HP and UHP rocks in the Western Alps. Bull. Soc. Geol. France. 172, 617–636.

Agard, P., Monié, P., Jolivet, L., Goffé, B., 2002. Exhumation of the Schistes Lustrés complex: in situ laser probe $^{40}Ar/^{39}Ar$ constraints and implications for the Western Alps. J. Metam. Geol. 20, 599–618.

Allard, T., Gautheron, C., Bressan-Riffel, S., Balan, E., Selo, M., Fernandes, B.S., Pinna-Jamme, R., Derycke, A., Morin, G., Taitson Bueno, G., Do Nascimento, N. R., 2018. Combined dating of goethites and kaolinites from ferruginous duricrusts. Deciphering the Late Neogene erosion history of Central Amazonia. Chem. Geol. 479, 136–150.

Alt, J.C., Schwarzenbach, E.M., Früh-Green, G.L., Shanks III, W.C., Bernasconi, S.M., Garrido, C.J., Crispini, L., Gaggero, L., Padron-Navarta, J.A., Marchesi, C., 2013. The role of serpentinites in cycling of carbon and sulfur: seafloor serpentinization and subduction metamorphism. Lithos 178, 40–54.

Ault, A.K., Gautheron, C., King, G.E., 2019. Innovations in (U-Th)/He, fission-track, and trapped-charge thermochronometry with applications to earthquakes, weathering, surface-mantle connections, and the growth and decay of mountains. Tectonics, DOI: 10.1029/2018TC005312.

Beucher, R., van der Beek, P., Braun, J. and Batt, G.E. (2012) Exhumation and relief development in the Pelvoux and Dora-Maira analysis and inversion of thermochronological age transects. J. Geophys. Res. 117, F03030.

595 Blackburn, T.J., Stockli, D.F., Walker, J.D., 2007. Magnetite (U-Th)/He dating and its
596 application to the geochronology of intermediate to mafic volcanic rocks. Earth Planet.
597 Sci. Lett. 259, 360–371.
598 Brunet, F., 2019. Hydrothermal production of H_2 and magnetite from steel slags: a geo-
599 inspired approach based on olivine serpentinization. Front. Earth Sci. 7,
600 https://doi.org/10.3389/feart.2019.00017
601 Cooperdock, E.H., Stockli, D.F., 2016. Unraveling alteration histories in serpentinites and
602 associated ultramafic rocks with magnetite (U–Th)/He geochronology. Geology 44,
603 967–970.
604 Cooperdock, E.H., Stockli, D.F., 2018. Dating exhumed peridotite with spinel (U–Th)/He
605 chronometry. Earth Planet. Sci. Lett. 489, 219–227.
606 Cooperdock, E.H., Ketcham, R.A., Stockli, D.F., 2019. Resolving the effects of 2D versus 3D
607 grain measurements on (U-Th)/He age data and reproducibility. Geochronology. 1, 17–
608 41.
609 Danišík, M., McInne, B.I.A., Kirkland, C.L., McDonald, B.J., Evans, N.J., Becker, T., 2017. Seeing
610 is believing: Visualization of He distribution in zircon and implications for thermal
611 history reconstruction on single crystals. Sci. Adv. 3, e1601121 DOI:
612 10.1126/sciadv.1601121
613 Dare, S.A.S., Barnes, S.J., Beaudouin, G., Méric, J., Boutroy, E., Potvin-Doucet, C., 2014. Trace
614 elements in magnetite as petrogenic indicators. Miner. Deposita 49, 785–796.
615 Debret B., Andreani M., Munoz M., Bolfan N., Carlut J., Nicollet C., Schwartz S., Trcera N,
616 2014. Iron oxidation state in serpentine during subduction: implications on the nature
617 of the released fluids. Earth Planet. Sci. Lett. 400, 206–218.

618 Deditius, A.P., Reich, M. Simon, A.C., Suvorova, A., Knipping, J., Roberts, M.P., Rubanov, S.,
619 Dodd, A., Saunders, M., 2018. Nanogeochemistry of hydrothermal magnetite. Contrib.
620 Mineral. Petrol. 173, 46, https://doi.org/10.1007/s00410-018-1474-1.
621 Djimbi, D.M., Gautheron, C., Roques, J., Tassan-Got, L., Gerin, C., Simoni, E., 2015. Impact of
622 apatite chemical composition on (U-Th)/He thermochronometry: an atomistic point of
623 view. Geochim. Cosmochim. Acta 167, 162–176.
624 Dodson, M.H., 1973. Closure temperature in cooling geochronological and petrological
625 systems. Contrib. Mineral. Petrol. 40, 259–274.
626 Dumont T., Schwartz S., Guillot S., Simon-Labric T., Tricart P., Jourdan S., 2012. Structural and
627 sedimentary records of the Oligocene revolution in the Western Alps. J. Geody. 56-57,
628 18-38.
629 Fanale, F.P., Kulp, J.L., 1962. The helium method and the age of the Cornwall Pennsylvania
630 magnetite. Econ. Geol. 57, 735–746.
631 Farley, K.A., Wolf, R.A., Silver, L.T., 1996. The effects of long alpha-stopping on (U-Th)/He
632 ages. Geochim. Cosmochim. Acta 21, 4223–4229.
633 Farley, K., 2002. (U-Th)/He dating: Techniques, calibrations, and applications, in:
634 geochemistry, R.i.m. (Ed.), Noble Gases in Geochemistry and Cosmochemistry, pp.
635 819–844.
636 Flowers, R., Ketcham, R.A., Shuster, D., Farley, K.A., 2009. Apatite (U-Th)/He
637 thermochronology using a radiation damage accumulation and annealing model.
638 Geochim. Cosmochim. Acta 73, 2347–2365.
639 Gallagher, K., Brown, R., Johnson, C., 1998. Fission track analysis and its applications to
640 geological problems. Annu. Rev. Earth Planet. Sci. 26, 519–572.

641 Gautheron, C., Tassan-Got, L., Barbarand, J., Pagel, M., 2009. Effect of alpha-damage
642 annealing on apatite (U-Th)/He thermochronology. Chem. Geol. 266, 166–179.
643 Gautheron, C., Tassan-Got, L., Ketcham, R.A., Dobson, K.J., 2012. Accounting for long alpha-
644 particle stopping distances in (U-Th-Sm)/He geochronology. 3D modeling of diffusion,
645 zoning, implantation, and abrasion. Geochim. Cosmochim. Acta 96, 44–56.
646 Gerin, C., Gautheron, C., Oliviero, E., Bachelet, C., Djimbi, D.M., Seydoux-Guillaume, A.M.,
647 Tassan-Got, L., Sarda, P., Roques, J., Garrido, F., 2017. Influence of vacancy damage on
648 He diffusion in apatite investigated at atomic to mineralogical scales. Geochim.
649 Cosmochim. Acta 197, 87–103.
650 Guenthner, W., Reiners, P.W., Ketcham, R., Nasdala, L., Giester, G., 2013. Helium diffusion in
651 natural zircon: radiation damage, anisotropy, and the interpretation of zircon (U-
652 Th)/He thermochronology. Am. J. Sci. 313, 145–198.
653 Guillot S., Schwartz S., Reynard B., Agard P., Prigent C., 2015. Tectonic significance of
654 serpentinites. Tectonophysics 646, 1–19.
655 Ketcham, R.A., Donelick, R.A., Carlson, W.D., 1999. Variability of apatite fission-track
656 annealing kinetics III: Extrapolation to geological time scales. Am. Mineral. 84, 1235–
657 1255.
658 Ketcham, R.A., 2005a. Computational methods for quantitative analysis of three-dimensional
659 features in geological specimens. Geosphere 1, 32–41.
660 Ketcham, R.A., 2005b. Forward and inverse modeling of low-temperature
661 thermochronometry data. Rev. Mineral. Geochem. 58, 275-314.
662 Ketcham, R.A., Gautheron, C., Tassan-Got, L., 2011. Accounting for long alpha-particle
663 stopping distances in (U-Th-Sm)/He geochronology: refinement of the baseline case.
664 Geochim. Cosmochim. Acta 75, 7779–7791.

Ketcham, R.A., van der Beek, P., Barbarand, J., Bernet, M., Gautheron, C., 2018. Reproducibility of Thermal History Reconstruction From Apatite Fission-Track and (U-Th)/He Data. Geochem. Geophys. Geosyst. 19, 2411–2436.

Ketcham, R.A., 2019, Fission track annealing: from geologic observations to thermal modeling. In: Fission track thermochronology and its application to geology (P. Fitzgerald and M. Malusa, eds.), Springer Textbooks in Earth Sciences, Geography and Environment, Springer, p. 49–75

Klein, F., Bach, W., McCollom, T.M., 2013. Compositional controls on hydrogen generation during serpentinization of ultramafic rocks. Lithos 178, 55–69.

Klein, F., Bach, W., Humphris, S., Kahl, W.A., Jöns, N., Moskowitz, B., Berquó, T., 2014. Magnetite in seafloor serpentinite – Some like it hot. Geology 42, 135–138.

Lafay, R., Deschamps, F., Schwartz, S., Guillot, S., Godard, M., Debret, B., Nicollet, C., 2013. High-pressure serpentinites, a trap-and-release system controlled by metamorphic conditions: Example from the Piedmont zone of the western Alps. Chem. Geol. 343, 38–54.

Lardeaux J.M., Schwartz S., Tricart P., Paul A., Guillot S., Béthoux N., Masson F. 2006. A crustal-scale cross-section of the southwestern Alps combining geophysical and geological imagery. Terra Nova. 18 (6), 412-422.

Lemoine, M., Bas, T., Arnaud-Vanneau, A., Arnaud, H., Dumont, T., Gidon, M., Bourbon, M., de Graciansky, P. C., Rudkiewicz, J. L., Megard-Galli, J., Tricart, P., 1986. The continental margin of the Mesozoic Tethys in the Western Alps. Mar. Petrol. Geol. 3, 179–199.

Li, X.P., Rahn, M. Bucher, K., 2004. Serpentinites of the Zermatt-Saas ophiolite complex and their texture evolution. J. Metam. Geol. 22, 159–177.

McDannell, K.T., Zeitler, P.K., Janes, D.J., Idleman, B.D., Fayon, A.K., 2018. Screening apatites for (U-Th)/He thermochronometry via continuous ramped heating: He age components and implications for age dispersion. Geochim. Cosmochim. Acta 223, 90–106.

Merkulova, M.V., Muñoz, M., Brunet, F., Vidal, O., Hattori, K., Vantelon, D., Trcera, N., Huthvelker, T., 2017. Experimental insight into redox transfer by iron- and sulfur-bearing serpentinite dehydration in subduction zones. Earth Planet. Sci. Lett. 479, 133-143.

Murakami, M., Yamada, R., Tagami, T., 2006. Short-term annealing characteristics of spontaneous fission tracks in zircon: A qualitative description. Chem. Geol. 227, 214–222.

Nadoll, P., Angerer, T., Mauk, J.L., French, D., Walshe, J., 2014. The chemistry of hydrothermal magnetite: a review. Ore Geol. Rev. 16, 1–32.

Pognante, U., Kienast, J.R., 1986. Blueschist and Eclogite Transformations in Fe-Ti Gabbros. A Case from the Western Alps Ophiolites. J. Petrol. 28, 271–292.

Rahn, M.K., Brandon, M., Batt, G.E., Garver, J., 2004. A zero-damage model for fission-track annealing in zircon. Am. Mineral. 89, 473–484.

Spiegel, C., Kohn, B., Belton, D., Berner, Z., Gleadow, A., 2009. Apatite (U-Th-Sm)/He thermochronology of rapidely cooled samples: The effect of He implantation. Earth Planet. Sci. Lett. 285, 105–114.

Schwartz, S., Allemand, P., Guillot, S., 2001. Numerical model of the effect of serpentinites on the exhumation of eclogitic rocks: insights from the Monviso ophiolitic massif (western Alps). Tectonophysics 342, 193–206.

711 Schwartz, S., Gautheron, C., Audin, L., Dumont, T., Nomade, J., Barbarand, J., Pinna-Jamme,
712 R., van der Beek, P., 2017. Foreland exhumation controlled by crustal thickening in the
713 Western Alps. Geology. 45, 139-142.
714 Schwartz, S., Lardeaux, J.M., Tricart, P., Guillot, S., Labrin, E., 2007. Diachronous exhumation
715 of HP–LT metamorphic rocks from south-western Alps: evidence from fission-track
716 analysis. Terra Nova 19, 133–140.
717 Schwartz, S., Tricart, P., Lardeaux, J. M., Guillot, S., Vidal O., 2009. Late tectonic and
718 metamorphic evolution of the Piedmont accretionary wedge (Queyras Schistes lustrés,
719 western Alps): Evidences for tilting during Alpine collision. Geol. Soc. Am. Bull. 121,
720 502–518.
721 Schwartz, S., Guillot, S., Reynard, B., Lafay, R., Debret, B., Nicollet, C., Lanari, P., Auzende,
722 A.L., 2013. Pressure-temperature estimates of the lizardite/antigorite transition in high
723 pressure serpentinites. Lithos 178, 197–210.
724 Shimazaki, H., 1998. On the Occurrence of Silician Magnetites. Resource Geology 48, 23–29.
725 Tricart P., Schwartz S., Sue C., Lardeaux J.M., 2004. Evidence of synextension tilting and
726 doming during final exhumation from analysis of multistage faults (Queyras Schistes
727 lustrés, Western Alps). J. Struct. Geol. 26, 1633–1645.
728 Tricart, P., Schwartz, S., 2006. A north - south section across the Queyras Schistes lustrés
729 (Piedmont zone, Western Alps): syncollision refolding of a subduction wedge. Eclogae
730 Geol. Helv. 99, 429–442.
731 Zhao, L., Paul A., Solarino S., Guillot S., Malusà M., Zheng T., Aubert C., Salimbeni S., Dumont
732 T., Schwartz S., Pondrelli S., Zhu R., Wang Q., 2015. First seismic evidence for
733 continental subduction beneath the Western Alps. Geology. 43, 815-818,
734 DOI:10.1130/G36833.1

735 Zeitler, P.K., Enkelmann, E., Thomas, J.B., Watson, E.B., Ancuta, L.D., Idleman, B.D., 2017.
736 Solubility and trapping of helium in apatite. Geochim. Cosmochim. Acta 209, 1–8.
737

Figure caption

Figure 1: (A) Geographical setting of the Alps showing the location of Fig. 1B. **(B)** Simplified structural and geological map of the Western Alps between France and Italy, with location of Figure 1C. **(C)** Structural sketch-map of the Schistes Lustrés units of Piedmont zone, with published apatite and fission tracks ages (modified from Schwartz et al., 2007) and location of the Rocher Blanc ophiolite massif (RB), with extrapolated AFT and ZFT ages (in *). The location of CG (Cirque de la Gavie) and RN (Rocca Nera) are also indicated. **(D)** Pressure-Temperature path from the Rocher Blanc ophiolite (modified from Schwartz et al., 2009).

Figure 2: Photographic views of the Rocher Blanc ophiolite massif, polished thin section of RB1 sample and SEM backscattered electron images. **(A)** Fe-Ti gabbro embedded in serpentinite and developing magnetite-bearing chloritoschist at its interface. **(B)** Millimeter scale euhedral magnetite crystals visible on outcrop indicated by white arrows. **(C)** Thin-section of the RB1 magnetite-bearing chloritoschist sample. The magnetite crystal analyzed is presented in Figure 3. **(D), (E)** and **(F)** are SEM-BSE images of the sample RB1. The sample presents two mineralogical zones (2 and 1), rich in titanite and ilmenite (D and E) and chlorite (F), respectively. Mag, Ttn, Ilm and Chl mean magnetite, titanite, ilmenite and chlorite.

Figure 3: Geochemical characterization of magnetite crystal from the chlorite-rich Zone 1 and titanite-rich Zone 2 shown in Fig. 2C (RB1-Mag1 and RB1-Mag5, Table 1). **(A,E)** EMP-SE image of the magnetite crystal with EMP elemental X-ray maps (1 µm beam size, 1.5 µm step size and 1s dwell time) and profile. **(B,F)** Si and V concentration in ppm along the profile.

761 **(C,G)** and **(D,H)** map of the Si and V concentration in ppm. Inclusions of silicate minerals
762 appear in white on the chemical maps.
763
764 **Figure 4:** In-situ U concentration of magnetite, chlorite and titanite from Zone 1 and Zone 2.
765 (**A**) Thin-section of the RB1 magnetite-bearing chloritoschist sample, with location of the U
766 analysis zones (**B**), (**C**) and (**D**). Zoom of the (**B**), (**C**) and (**D**) areas and U content in ppb.
767
768 **Figure 5:** Magnetite (U-Th-Sm)/He ages from Rocher Blanc ophiolite. **(A)** and **(B)** are 3D
769 reconstructions from CT-scan images of each euhedral and pseudo-euhedral crystals. **(C)**
770 MgHe age as a function of the sphere equivalent radius (Rs) estimated from CT-scan analysis
771 (Ketcham, 2005a; Cooperdock et al., 2019). The AFT and ZFT age ranges from Schwartz et al.
772 (2007) and shown in Figure 1C are shown.
773
774 **Figure 6:** Pressure-temperature-time pathway record by the RB ophiolite and magnetite
775 growth condition. (**A**) Pressure-Temperature-time path of the HP-LT Rocher Blanc ophiolite
776 modified from Schwartz et al. (2009; 2013). The AFT and ZFT estimated ages from RB (Fig.
777 1C), MgHe ages from euhedral magnetites are reported for their associated closure
778 temperature condition (Blackburn et al., 2007; Gallagher et al., 1998; Ketcham, 2019). The
779 age of HP conditions are taken from Agard et al. (2002). (**B**) Sketch of magnetite crystals
780 growth during the retrograde pathway in three main steps, from (I) blueschist conditions
781 (BS), (II) High-Pressure greenschist (HP-GS) and (III) Low-Pressure greenschist (LP-GS)
782 conditions. Zones 1 and 2 refer to the initial magmatic sites with augite-plagioclase and Fe-Ti
783 oxide (ilmenite) respectively. (I) The HP blueschist conditions are marked by the partial
784 mineralogical transformation of augite to aegirine, and the development of glaucophane and

785 zoisite in the plagioclase site (Pognante et al., 1986). In Zone 2, ilmenite is progressively
786 transformed to titanite. (II) The HP greenschist conditions are marked by the progressive
787 destabilization of augite-aegirine, glaucophane, and zoisite to chlorite and magnetite in Zone
788 1, whereas, ilmenite continues to be destabilized in titanite and ± magnetite and chlorite.
789 The magnetite grains show low Si content whatever the considered zones. (III) Finally, the LP
790 greenschist facies conditions, show the pervasive development of the chlorite and magnetite
791 in the two zones. In the zone 2, only relics of ilmenite remain locally in the core of titanite
792 crystals. The magnetites present higher Si content.
793
794 **Figure 7:** Thermochronological data inversion modeling of the HP-LT Rocher Blanc RB
795 ophiolite using HeFTy software (Ketcham, 2005). **(A).** T-t pathways obtained for MgHe data
796 inversion only. **(B).** T-t pathways obtained for AFT and ZFT data inversion only. **(C).** T-t paths
797 obtained for joint AFT, ZFT and MgHe data inversion.
798
799 **Figure 8:** Schematic evolution of the Western Alps between France and Italy ~20 Ma ago and
800 at present-day. At ~20 Ma, the Penninic Frontal Thrust (PFT) is already active since 10 Myr
801 associated with the mantellic upward indentation, and the AFT-ZFT and MgHe dated
802 samples have started to be exhumed in the brittle condition (above 250°C). The samples
803 record differential exhumation related with the westward tilting and uplift. One
804 representative sample from Dora Maira massif is represented, where AFT ages of 20-25Ma
805 have recorded by Beucher et al. (2012).
806
807 **Figure S1:** Thermochronological data inversion modeling of the HP-LT Rocher Blanc RB
808 ophiolite using HeFTy software (Ketcham, 2005). T-t paths obtained using AFT and ZFT data

809 from sample CG **(A, B, C)**, sample RB **(D, E, F)**, RN sample **(G, H, I)**, combined without or with
810 MgHe data. **(J-K)** Weighted model Tt paths resumed results for CG, RB and RN samples,
811 without or with MgHe data. **(L).** Tt pathway model obtained for MgHe data inversion only.
812
813 **Table 1:** Elemental concentration in ppm obtained on four representative magnetite crystals
814 from zone 1 of the RB1 sample.
815
816 **Table 2:** In-situ U and Th concentrations obtained by LA-ICP-MS in sample RB1 (thick section).
817
818 **Table 3:** CT-scan and (U-Th-Sm)/He results of the magnetite-bearing chloritoschist RB1
819 sample
820
821 **Table 4:** Thermal History Inverse Modeling Parameters

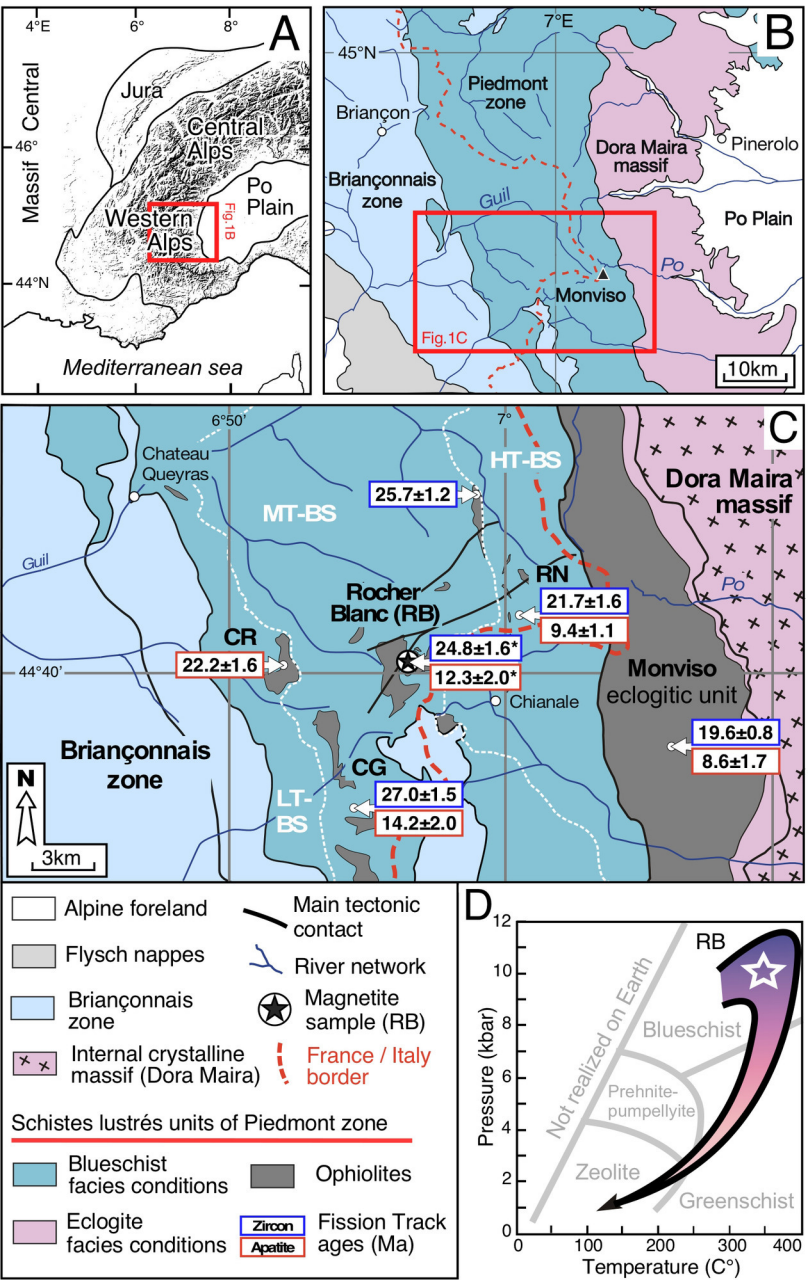
A
4°E
6°
8°
Central Massif
46°
44°N
Jura
Central Alps
Western Alps
Fig.1B
Po Plain
Mediterranean sea
B
7°E
45°N
Piedmont zone
Briançon
Pinerolo
Dora Maira massif
Briançonnais zone
Guil
Po Plain
Po
Monviso
Fig.1C
10km
C
6°50'
7°
Chateau Queyras
HT-BS
25.7±1.2
MT-BS
Dora Maira massif
Guil
RN
21.7±1.6
Rocher Blanc (RB)
9.4±1.1
Po
CR
22.2±1.6
24.8±1.6*
12.3±2.0*
44°40'
Chianale
Monviso eclogitic unit
19.6±0.8
8.6±1.7
Briançonnais zone
CG
27.0±1.5
LT-BS
14.2±2.0
N
3km
Alpine foreland
Flysch nappes
Briançonnais zone
Internal crystalline massif (Dora Maira)
Main tectonic contact
River network
Magnetite sample (RB)
France / Italy border
Schistes lustrés units of Piedmont zone
Blueschist facies conditions
Ophiolites
Eclogite facies conditions
Zircon
Apatite
Fission Track ages (Ma)
D
Pressure (kbar)
Temperature (C°)
RB
Blueschist
Not realized on Earth
Prehnite-pumpellyite
Zeolite
Greenschist
0
2
4
6
8
10
12
0
100
200
300
400

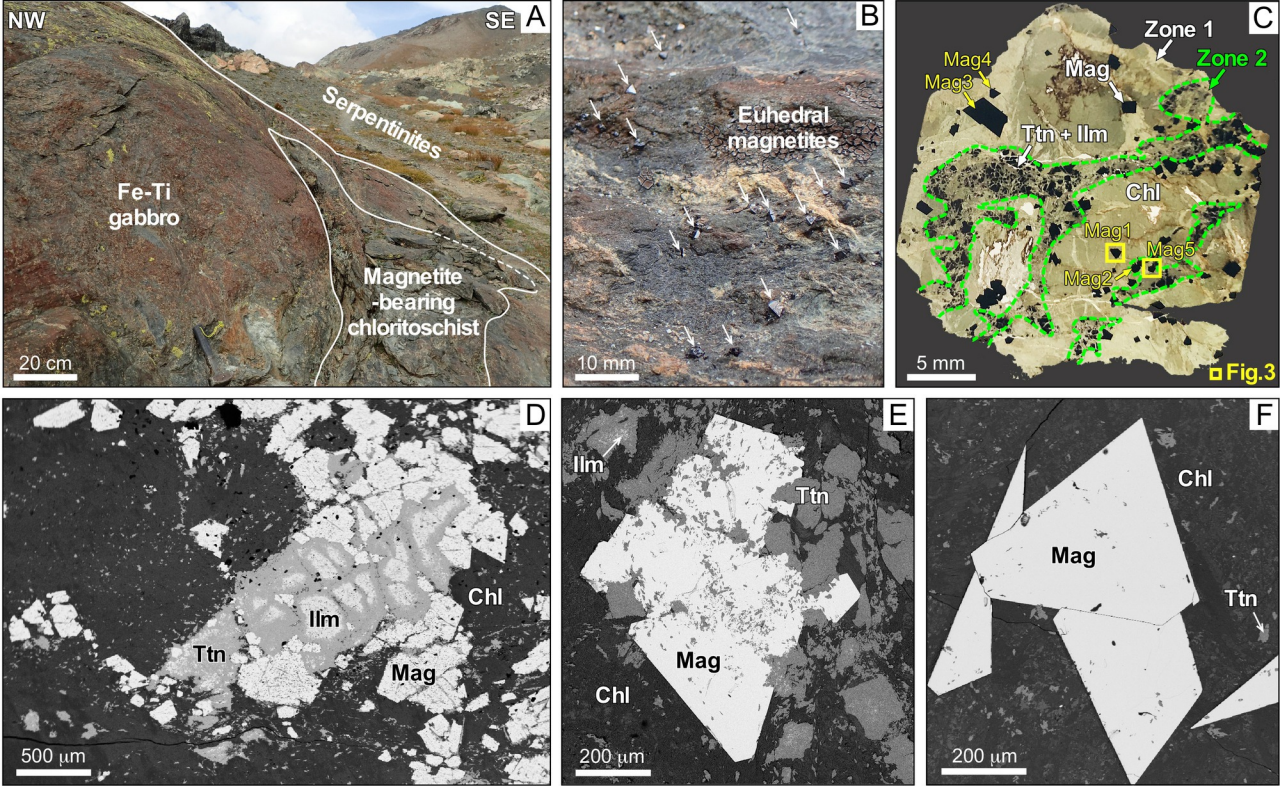
NW
SE
A
Serpentinites
Fe-Ti
gabbro
Magnetite
-bearing
chloritoschist
20 cm
B
Euhedral
magnetites
10 mm
C
Zone 1
Zone 2
Mag4
Mag3
Mag
Ttn + Ilm
Chl
Mag1
Mag5
Mag2
5 mm
Fig.3
D
Ilm
Chl
Ttn
Mag
500 μm
E
Ilm
Ttn
Mag
Chl
200 μm
F
Chl
Mag
Ttn
200 μm

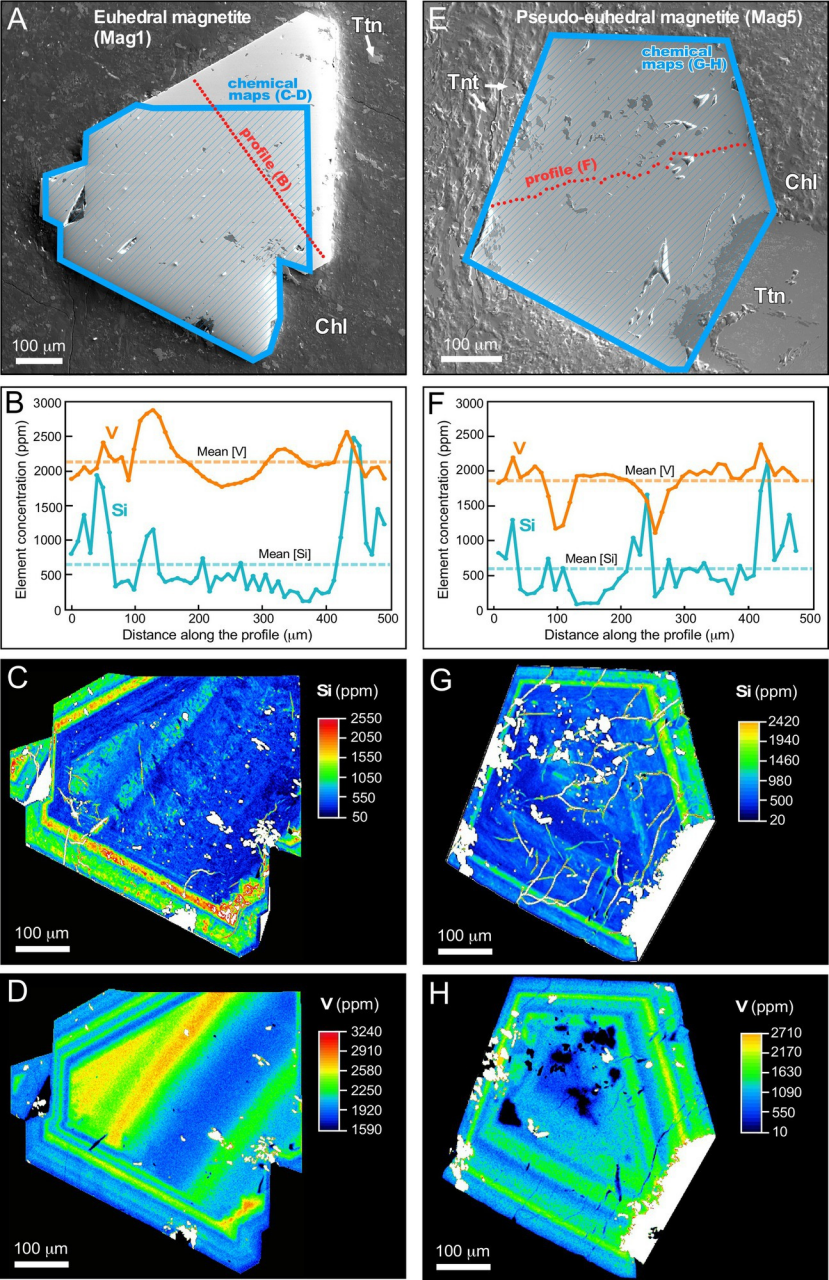
A
Euhedral magnetite (Mag1)
Ttn
chemical maps (C-D)
profile (B)
Chl
100 μm
E
Pseudo-euhedral magnetite (Mag5)
chemical maps (C-H)
Tnt
profile (F)
Chl
Ttn
100 μm
B
V
Si
Mean [V]
Mean [Si]
Element concentration (ppm)
Distance along the profile (μm)
F
V
Si
Mean [V]
Mean [Si]
Element concentration (ppm)
Distance along the profile (μm)
C
Si (ppm)
2550
2050
1550
1050
550
50
100 μm
G
Si (ppm)
2420
1940
1460
980
500
20
100 μm
D
V (ppm)
3240
2910
2580
2250
1920
1590
100 μm
H
V (ppm)
2710
2170
1630
1090
550
10
100 μm

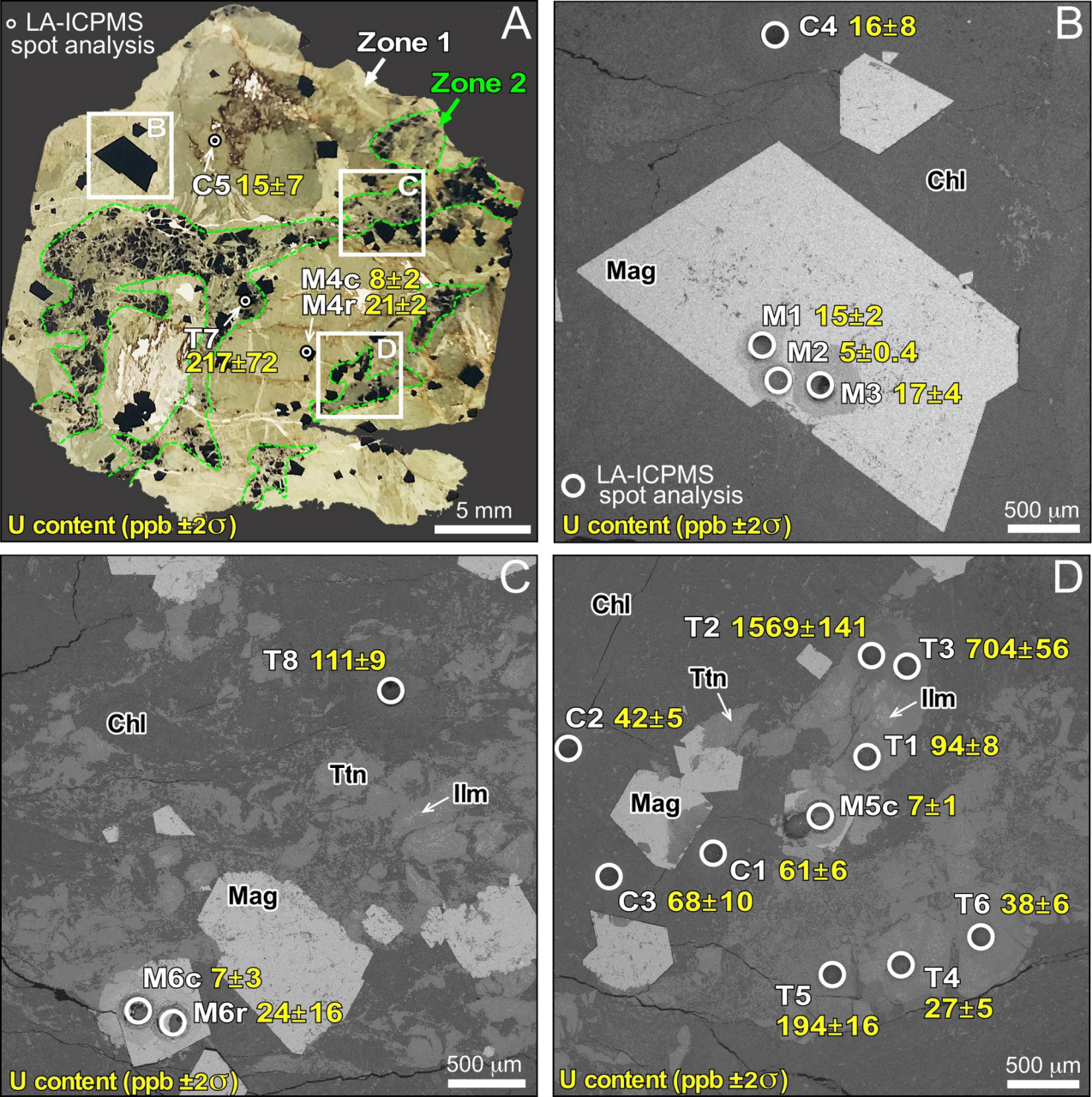
A
LA-ICPMS spot analysis
Zone 1
Zone 2
B
C5 15±7
C
M4c 8±2
M4r 21±2
T7 217±72
D
5 mm
U content (ppb ±2σ)
B
C4 16±8
Chl
Mag
M1 15±2
M2 5±0.4
M3 17±4
LA-ICPMS spot analysis
500 μm
U content (ppb ±2σ)
C
T8 111±9
Chl
Ttn
Ilm
Mag
M6c 7±3
M6r 24±16
500 μm
U content (ppb ±2σ)
D
Chl
T2 1569±141
T3 704±56
Ttn
Ilm
C2 42±5
T1 94±8
Mag
M5c 7±1
C1 61±6
C3 68±10
T6 38±6
T5 194±16
T4 27±5
500 μm
U content (ppb ±2σ)

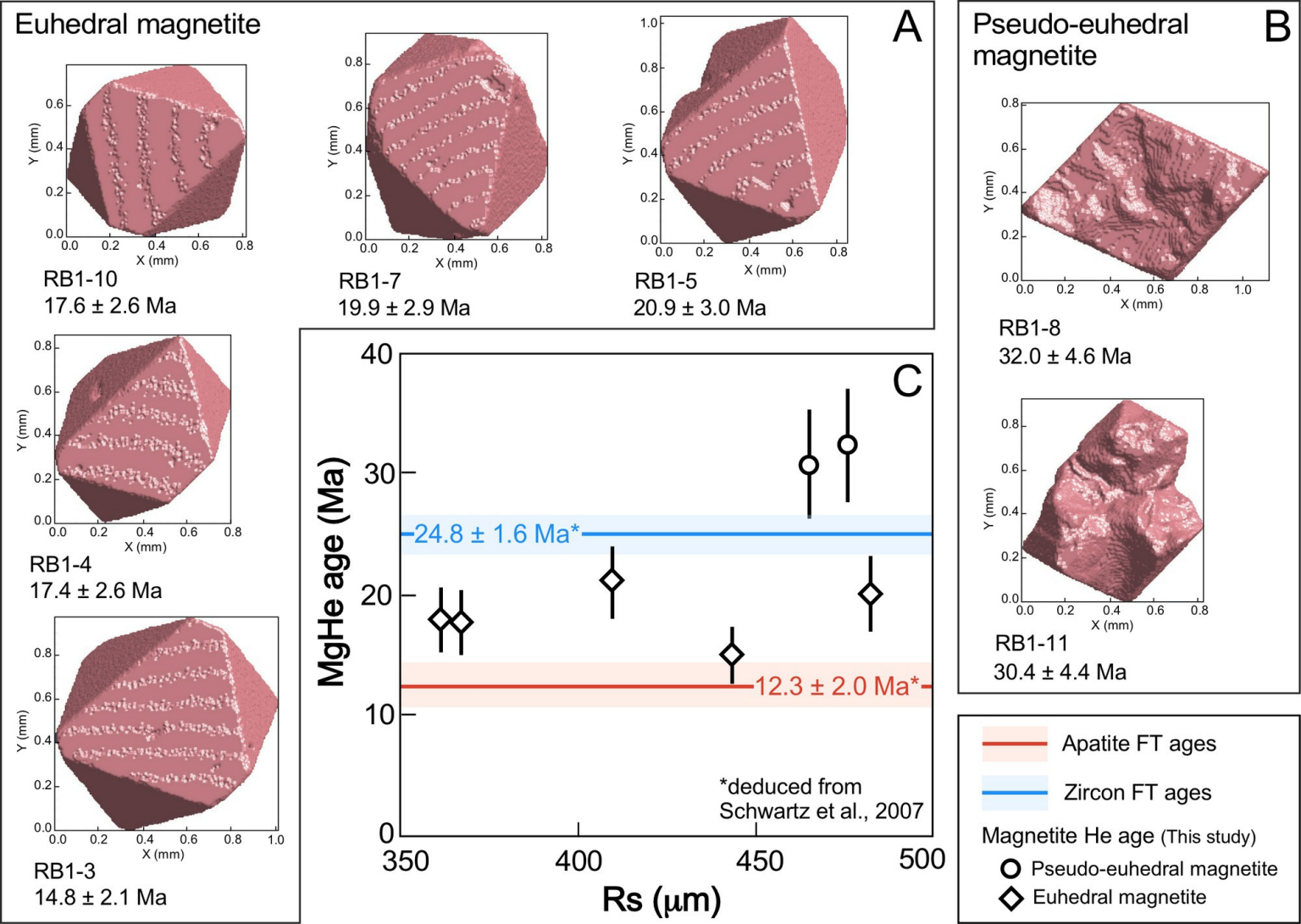
Euhedral magnetite
A
RB1-10
17.6 ± 2.6 Ma
RB1-7
19.9 ± 2.9 Ma
RB1-5
20.9 ± 3.0 Ma
RB1-4
17.4 ± 2.6 Ma
RB1-3
14.8 ± 2.1 Ma
Pseudo-euhedral magnetite
B
RB1-8
32.0 ± 4.6 Ma
RB1-11
30.4 ± 4.4 Ma
C
MgHe age (Ma)
Rs (μm)
24.8 ± 1.6 Ma*
12.3 ± 2.0 Ma*
*deduced from Schwartz et al., 2007
Apatite FT ages
Zircon FT ages
Magnetite He age (This study)
Pseudo-euhedral magnetite
Euhedral magnetite

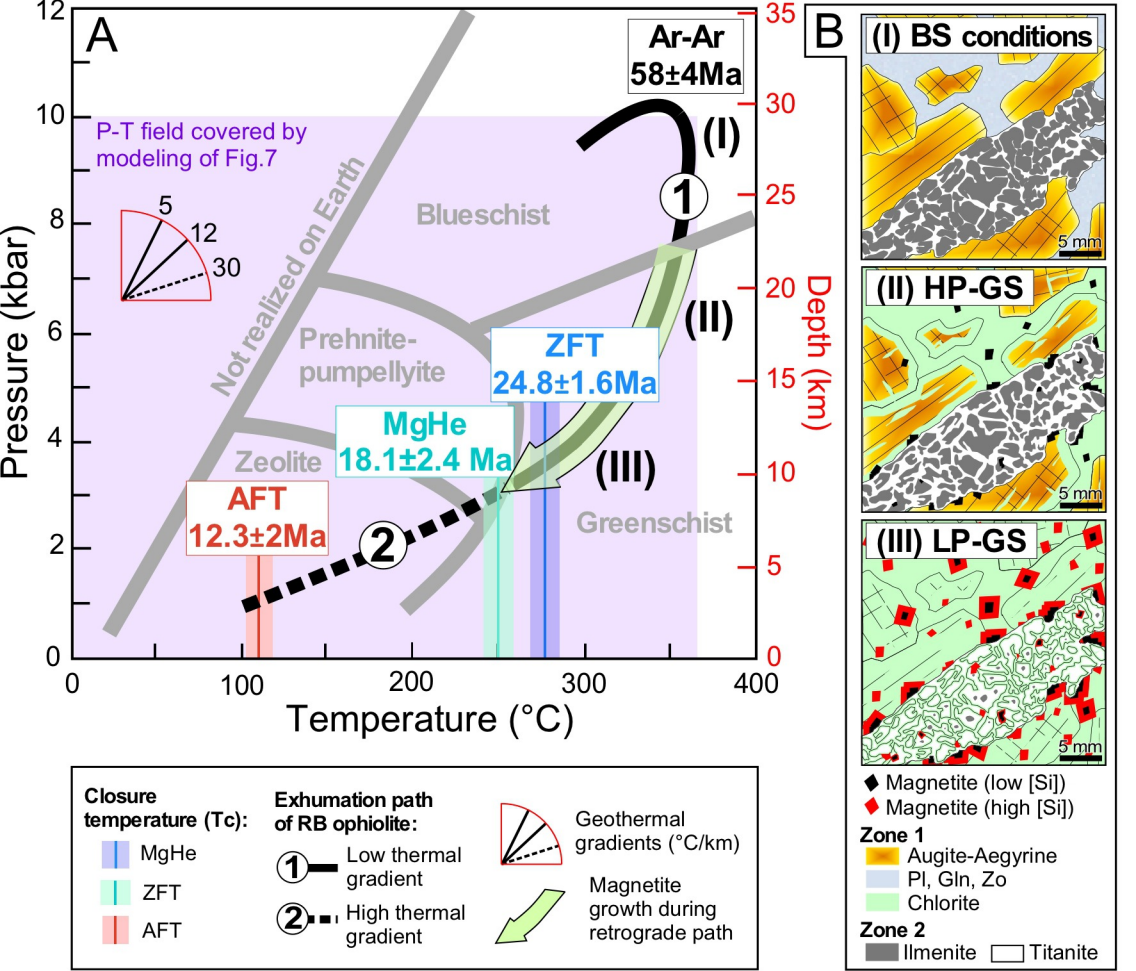
A
Ar-Ar
58±4Ma
(I)
1
P-T field covered by
modeling of Fig.7
5
12
30
Blueschist
Not realized on Earth
Prehnite-
pumpellyite
(II)
ZFT
24.8±1.6Ma
MgHe
18.1±2.4 Ma
Zeolite
(III)
AFT
12.3±2Ma
2
Greenschist
Pressure (kbar)
Depth (km)
Temperature (°C)
0
2
4
6
8
10
12
0
5
10
15
20
25
30
35
0
100
200
300
400
B
(I) BS conditions
(II) HP-GS
(III) LP-GS
5 mm
Magnetite (low [Si])
Magnetite (high [Si])
Zone 1
Augite-Aegyrine
Pl, Gln, Zo
Chlorite
Zone 2
Ilmenite
Titanite
Closure
temperature (Tc):
MgHe
ZFT
AFT
Exhumation path
of RB ophiolite:
1
Low thermal
gradient
2
High thermal
gradient
Geothermal
gradients (°C/km)
Magnetite
growth during
retrograde path

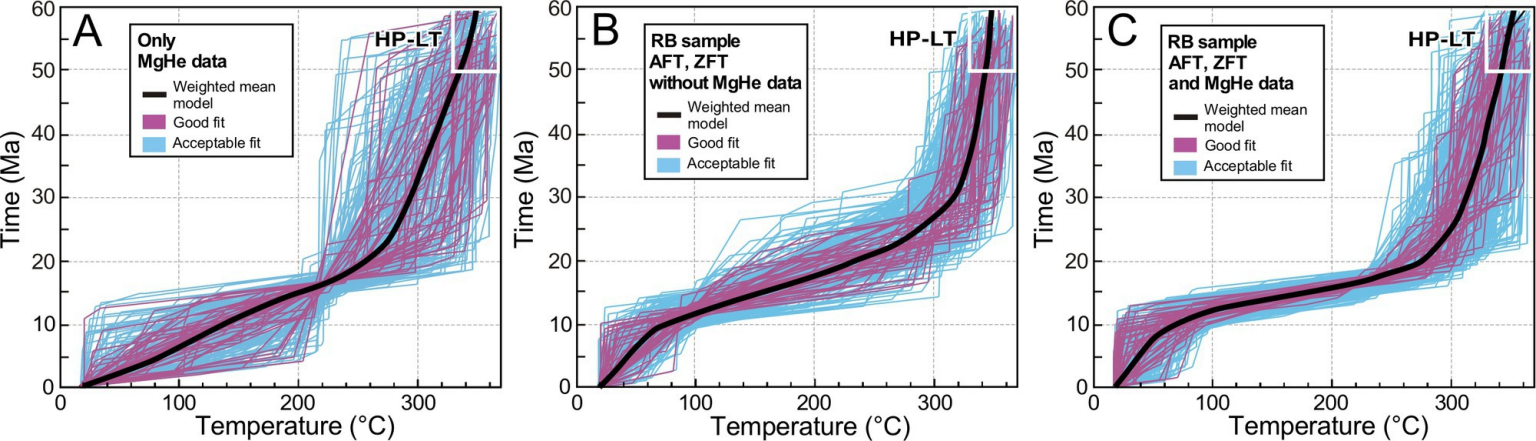
A
Only
MgHe data
Weighted mean
model
Good fit
Acceptable fit
HP-LT
Time (Ma)
Temperature (°C)
B
RB sample
AFT, ZFT
without MgHe data
Weighted mean
model
Good fit
Acceptable fit
HP-LT
Time (Ma)
Temperature (°C)
C
RB sample
AFT, ZFT
and MgHe data
Weighted mean
model
Good fit
Acceptable fit
HP-LT
Time (Ma)
Temperature (°C)

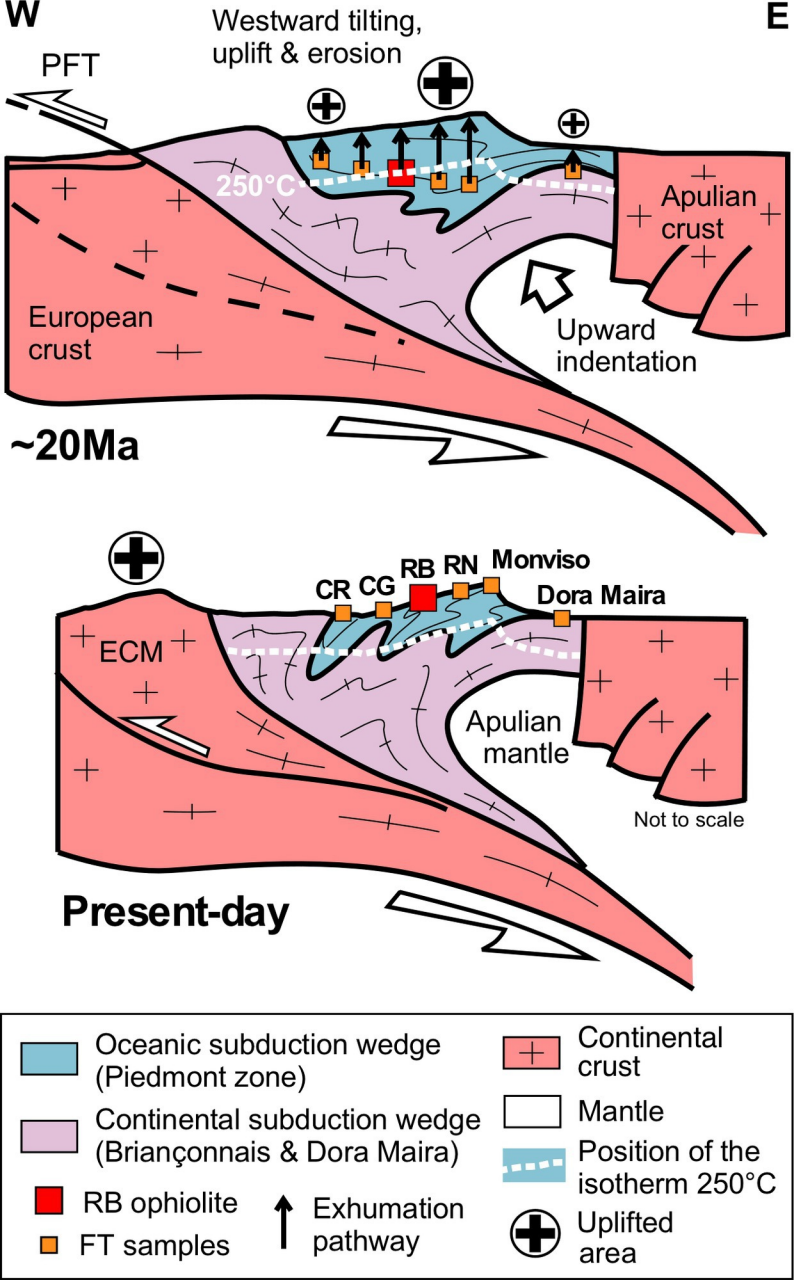
W
E
Westward tilting,
uplift & erosion
PFT
250°C
Apulian
crust
European
crust
Upward
indentation
~20Ma
CR CG RB RN Monviso
Dora Maira
ECM
Apulian
mantle
Not to scale
Present-day
Oceanic subduction wedge
(Piedmont zone)
Continental subduction wedge
(Briançonnais & Dora Maira)
RB ophiolite
FT samples
Exhumation
pathway
Continental
crust
Mantle
Position of the
isotherm 250°C
Uplifted
area

Table 1: Elemental concentration in ppm obtained on representative magnetite crystals from zone 1 and zone 2 of the RB1 sample.

Element	Si	Ti	Cr	V	Mn	Mg
Detection Limit (ppm)	**24**	**30**	**30**	**30**	**35**	**25**
Euhedral magnetite						
RB1-Mag1 (n=76) Size 500 µm Profile B – Fig. 3	680±474	138±102	55±11	2119±244	432±35	B.d.l.
RB1-Mag3 (n=69) Size 650 µm	1019±638	72±48	48±10	1669±267	420±24	B.d.l.
RB1-Mag4 (n=61) Size 600 µm	744±349	60±38	45±10	1802±230	429±19	B.d.l.
Pseudo-euhedral magnetite						
RB1-Mag2 (n=53) Size 550 µm	993±650	59±31	43±11	1653±329	418±34	B.d.l.
RB1-Mag5 (n=42) 480 µm Profile F – Fig. 3	608±456	n.a.	n.a.	1863±257	n.a.	n.a.
RB1 (n=301)	**809±513**	**82±55**	**48±10**	**1821±265**	**425±28**	**B.d.l.**

B.d.l.: Below detection limits

n.a. not analyzed

Table 2: In-situ U and Th concentrations obtained by LA-ICP-MS in sample RB1 (thick section).

Magnetite	**M1**	**M2**	**M3**	**M4c$^{\$}$**	**M4r$^{\$}$**	**M5c**	**M6c**	**M6r**
	Zone 1 - euhedral mag.					Zone 2 - pseudo euhedral mag.		
U ± 2σ (ppb)	15±2	5±0.4	17±4	8±2	21±2	7±1	7±3	24±16
Th ± 2σ (ppb)	3±3	bdl	6±3	1±0.7	6±9	3±0.6	4±1	bdl
Titanite	**T1**	**T2**	**T3**	**T7**	**T8**	**T4***	**T5***	**T6***
	Zone 2							
U ± 2σ (ppb)	94±8	1569±141	704±56	217±72	111±9	27±5	194±16	38±6
Th ± 2σ (ppb)	28±22	628±546	109±9	163±117	4±1	4±1	36±3	6±1
Chlorite	**C4**	**C5**	**C1**	**C2**	**C3**			
	Zone 1		Zone 2					
U ± 2σ (ppb)	16±8	15±7	61±6	42±5	68±10			
Th ± 2σ (ppb)	5±1	13±5	7±1	13±3	17±12			

c$^{\$}$ and r$^{\$}$ mean magnetite core and rim

* Mn-rich titanite

bdl= below detection limit

Table 3: CT-scan and (U-Th-Sm)/He results of the magnetite-bearing chloritoschist RB1 sample

Aliquot	Volume (mm^3)	Surface area (mm^2)	Rs (μm)	F_T	Mass (mg)	^4He (pmol)	^{238}U (ng)	^{232}Th (ng)	^{147}Sm (ng)	^4He±s (pmol/g)	^{238}U (ppb)	^{232}Th (ppb)	^{147}Sm (ppb)	eU (ppb)	Th/U	Raw date (Ma)	Corrected date±s (Ma)
Euhedral magnetite																	
RB1-3	0.29	2.72	444	0.98	1.54	2.33×10^{-3}	0.025	0.020	0.018	1.49±0.03	16.2	13.0	11.7	19	0.8	14.4±2.2	14.8±2.1
RB1-4	0.16	1.82	368	0.97	0.84	1.85×10^{-3}	0.019	0.007	0.021	2.18±0.04	22.7	8.4	25.1	25	0.4	16.9±2.5	17.4±2.6
RB1-5	0.21	2.28	410	0.97	1.12	1.16×10^{-3}	0.009	0.007	0.015	0.88±0.02	7.8	6.5	13.3	9	0.8	20.4±3.1	20.9±3.1
RB1-7	0.25	2.46	483	0.98	1.32	4.71×10^{-3}	0.038	0.027	0.075	1.85±0.04	28.7	20.2	56.9	34	0.7	19.5±2.9	19.9±2.9
RB1-10	0.16	1.82	362	0.97	0.85	2.03×10^{-3}	0.020	0.009	0.015	2.31±0.05	23.2	11.2	17.5	26	0.5	17.1±2.6	17.6±2.6
Pseudo-euhedral magnetite																	
RB1-8	0.18	2.12	477	0.98	0.94	3.23×10^{-3}	0.016	0.012	0.020	3.26±0.07	17.3	12.3	21.9	20	0.7	31.3±4.7	32.0±4.8
RB1-11	0.13	1.80	466	0.98	0.71	1.60×10^{-3}	0.008	0.007	0.004	2.39±0.05	11.7	9.7	6.2	14	0.8	29.7±4.5	30.4±4.6

Rs and F_T are the sphere equivalent radius and alpha ejection factor.

(U-Th-Sm)/He date has been corrected from alpha ejection factor (F_T) (Ketcham et al., 2011).

Table 4: Thermal History Inverse Modeling Parameters

1. Thermochronologic data	
Samples and data used	AFT and ZFT data from Schwartz et al. (2007)
	MgHe data from this paper: Table 2, samples RB1-3, 4, 5, 7, and 10
Data treatment: Dates, uncertainties, and other relevant constraints	
AFT data	Kinetics: Apatite assumed to have Cl=0 apfu
	Uncertainty model: Asymmetric 95% bounds
ZFT data	Initial mean track length: N/A; no track length data available
	Uncertainty model: Asymmetric 95% bounds
MgHe data	Uncertainty model: Uniform 15% (1SE) uncertainty
2. Additional geologic information and constraint placement	
Present-day temperature	20°C
Initial constraint	Assumed peak HP-LT conditions: 350±20°C at 58±4 Ma
T-t path complexity	HeFTy code E3/50: Paths episodic, halved 3 times, with maximum cooling rate 50°C/m.y.
3. System- and model-specific parameters	
AFT annealing model: Ketcham et al. (1999)	
ZFT annealing model: Ketcham (2019)	
MgHe diffusion parameters: Blackburn et al. (2007)	
Modeling code: HeFTy v1.9.3	
Statistical fitting criteria: HeFTy default	
Ending condition: Models run until 50 good fits found	